Article:
Mullis, AM orcid.org/0000-0002-5215-9959 and Haque, N (2020) Evidence for dendritic fragmentation in as-solidified samples of deeply undercooled melts. Journal of Crystal Growth, 529. ARTN: 125276. ISSN 0022-0248

https://doi.org/10.1016/j.jcrysgro.2019.125276

Evidence for dendritic fragmentation in as-solidified samples of deeply undercooled melts

Andrew M Mullis[1] *& Nafisul Haque*[1,2]

[1]School of Chemical and Process Engineering, University of Leeds, Leeds, UK
[2] Department of Metallurgical Engineering, NEDUET, University Road, Karachi 75270, Pakistan

Corresponding Author: A.M.Mullis@leeds.ac.uk

Abstract. The congruently melting, single phase intermetallic β-Ni_3Ge has been subject to rapid solidification via drop-tube processing. We establish that the rapidly solidified material growing during the recalescence phase of solidification can be distinguished from the post-recalescence material in the as-solidified sample by the degree of chemical ordering displayed. This can in turn be used to visualize the material from the recalescence phase of solidification. At intermediate cooling rates this recalescence material consists of fragmented dendrites. The occurrence of fragmentation is compared against established theoretical models based on the growth of Rayleigh instabilities with excellent agreement being found. EBSD mapping is used to establish the relationship between these dendritic fragments and the final grain size distribution. The dendritic fragments are found to be poor nuclei for new grains and the fragmented dendrites do not consistently give rise to classical grain refined structures.

Keywords: A1. Dendrites; A1. Crystallites; A1. Etching; A1. Fluid flow.

1. Introduction

Spontaneous grain refinement[1, 2, 3] (SGR) is defined as an abrupt reduction in grain size during the solidification of deeply undercooled metallic melts above some critical undercooling, normally denoted as ΔT^*. First investigated by Walker[4] in pure Ni, ΔT^* was determined as 140 – 150 K, above which the coarse columnar grain structure transformed to a fine grained equiaxed structure, with at least one order of magnitude reduction in grain size. Similar behaviour was identified in pure Co, with a value for ΔT^* of $\approx$180 K being reported. Subsequently SGR has been reported in a range of other pure metals[2, 5, 6].

This effect is also found in a wide range of alloy systems[7, 8, 9, 10], although an evolutionary sequence of a more complex character is often observed with increasing undercooling. At low undercooling, a columnar growth pattern is found, this giving way to an equiaxed grain structure as the undercooling increases beyond a critical value, ΔT_1^*. A second region of columnar growth is observed at higher undercooling, which is again transformed to a fine grained equiaxed structure above a second critical undercooling, ΔT_2^*.

Dendrite fragmentation was proposed at an early stage as a possible mechanism, wherein such fragments would provide copious heterogeneous nucleation sites for the growth of new grains[11]. Kattamis and Flemings[12] gave support this idea, finding branched dendritic fragments in the solute segregation patterns of grain refined alloys. Shaeffer and Glicksman[13] found that, soon after forming, dendrites growing at the surface of Sn–Bi alloys completely fragmented. Over thirty years later, Cochrane *et al*.[14] found that both fragmentation and recrystallisation could result in spontaneous grain refinement in dilute Cu alloys. More recently, a range of models have been proposed including remelting of dendritic seaweed[15, 16] and mixed mode mechanisms[17, 18] in which remelting of dendrites, remelting of dendritic seaweed and recrystallization all operate in different undercooling ranges.

The model for dendritic fragmentation elaborated by Karma[19] and by Schwarz *et al*.[20] is the most widely recognised model for spontaneous grain refinement. It invokes the growth of a Rayleigh type instability as the underlying mechanism for breakup. As such, the model of Karma shares some similarities with an earlier work by Cline[21], in which the latter had recourse to the same kind of morphological instability in order to explicate the fragmentation of rod-like eutectics.

The Schwarz model suggests that two characteristic timescales are important when considering whether breakup will occur. The first is the breakup time, τ_{bu}. This is the time that is required for fragmentation of the dendrite side-branches due to the growth of the Rayleigh instability. τ_{bu} is a monotonic function of the dendrite trunk radius, with small radii giving short breakup times. The second timescale is the plateau time, τ_{pl}. This is the time the melt remains at, or around, the melting temperature following recalescence and is determined solely by the macroscopic heat extraction rate. According to the Schwarz model, grain refinement occurs when $\tau_{bu} < \tau_{pl}$. This corresponds to the tip radius being below some critical value, R_{Tip}^*, which was also invoked to explain the single SGR transition in pure metals and the double SGR transition in alloys. Specifically, R_{Tip} passes through a local minimum at low undercoolings in alloy systems[22], which Schwarz relate to the ΔT_1^* transition. For the system used as an example

by Schwarz *et al.*[20], $Ni_{70}Cu_{30}$, growth of the Rayleigh instability was solute controlled giving breakup times that ranged from < 1 s, for undercoolings giving rise to small R_{Tip}, to > 20 s when R_{Tip} was large. As such, high cooling rates can suppress fragmentation, and Schwarz *et al.* observed that the ΔT_1^* transition was suppressed in their system for $\dot{T} > 1000$ K s^{-1}.

However, despite the reliance of the model on dendrite fragmentation, instances where evidence of the fragmentation process survive in the as-solidified sample are rare. Partly this is because the as-solidified samples of most crystalline alloys show multiple interpenetrating dendrites, makeing the analysis of these samples, and the subsequent identification of fragmentation difficult, partly it is that the high undercoolings required to access this type of dendrite fragmentation are not normally encountered. Heringer *et al*.[23] predicted that remelting should occur in Al-based alloys, with the extent of remelting increasing as the melt undercooling increased. EBSD analysis appeared to confirm remelting and detachment of secondary arms, which displayed a slight misorientation with respect to the primary dendritic trunks[24]. Peng *et al*.[25] observed clear evidence of the remelting and fragmentation of secondary dendrite arms in as-solidified Sn-36at.% Ni alloy, with many of the secondary arms becoming detached from their parent trunks and subsequently partially spheroidized (see e.g. their Figure 2c1). Moreover, although these authors do not comment upon it, some of their micrographs show primary dendrite trunks also close to being fragmented (see e.g. their Figure 4c). Huo *et al*.[26] observed the detachment and remelting of secondary dendrite arms in the as-solidified microstructure of directionally solidified Ni superalloys. Interestingly, it was the intended single crystal nature of the product that enabled them to detect such remelting and subsequently identify the fragments in EBSD analysis. They found that, in general, the fragments did not migrate far from their parent trunks and that despite small rotations of the fragments they frequently did not initiate the formation of new grains. Further evidence of dendrite fragmentation is presented by Hernando *et al*.[27] in as-solidified hypo-eutectic cast iron. In particular, they observe complete fragmentation of a primary dendrite trunk which appears as a linear array of uniform spherical particles. Its dendritic origin is however given away by the secondary arms radiating away from the line of fragments.

In contrast, the observation of dendrite fragmentation via *in situ* x-ray observation, particularly with the use of synchrotron radiation, has become widespread in recent years. Using automated image processing Liotti *et al*.[28] have demonstrated fragmentation rates in directionally solidified samples which are of the order 10^9 fragmentation events per m^3 per s. Evidence for the detachment and spheriodization of secondary dendrite arms from *in situ* observation has

been provided by a number of authors including Shevechenko *et al*.[29] in a model Ga-In alloy, Zeng *et al*.[30] in SAC Pb-free solder alloys and Yasuda *et al*.[31] in a 0.45 wt.% C steel.

In this article we present an analysis of rapidly solidified, single phase, Ni_3Ge processed via the drop-tube technique. A range of microstructures have previously been reported[32, 33] in this system as the cooling rate is increased, although here we focus on a property of the system that allows the breakup of dendrites into spherical fragments to be observed in the as-solidified material. Such dendritic fragmentation is observed at cooling rates in the range 2800–7800 K s^{-1}, corresponding to droplets sizes of 300–150 μm. Specifically, due to disorder trapping at high undercooling, material that solidifies during the recalescence phase of solidification grows as a disordered, fcc, solid solution. Conversely, material that grows post-recalescence grows to the ordered $L1_2$ variant of the same compound. During subsequent etching the disordered form of the material is attacked readily by the etchant, whereas the ordered compound appears unaffected by it, giving a means to obtain direct contrast between the recalescence and post-recalescence material in the as-solidified sample. As far as we are aware, this material is unique in being able to distinguish between these two stages of the rapid solidification process. Although we utilise this property here to investigate dendrite fragmentation other applications could be envisaged.

2. Experimental Methods

According to the thermodynamic assessment given by Nash & Nash[34] the β-Ni_3Ge compound has a homogeneity range of 22.5 to 25.0 at. % Ge, melting congruently at 1405 K. Upon equilibrium solidification it grows to the chemically ordered $L1_2$ structure directly from the melt, although disorder trapping can be occasioned by rapid solidification, wherein growth to a random fcc solid-solution occurs. It is shown by Ahmad *et al*.[35] that this occurs for undercoolings of 168 K or greater, corresponding to a critical growth velocity of 0.22 m s^{-1}.

The β-Ni_3Ge compound was produced by arc-melting Ni & Ge together in the correct proportions under a protective Ar atmosphere. XRD analysis, performed using a PANalytical Xpert Pro, was used to confirm the phase composition of the subsequent ingot. Once the material was confirmed to be single phase, rapid solidification processing was undertaken using the Leeds 6.5 m drop-tube.

The arc-melt ingot, which was approximately 9.6 g in mass, was loaded into an alumina crucible which had three, 300 μm, laser drilled holes in the base. The sample was melted by using

induction heating, with a graphite suseceptor being utilised in order to achieve efficient RF coupling. Once the desired temperature of 1480 K (1207 °C) (corresponding to 75 K superheat) was achieved, the crucible was pressurized to 400 kPa wherein a spray of fine droplets is produced. These solidify in free-fall down the tube, which is maintained at a pressure of 50 kPa with a high purity inert atmosphere. Further details of this drop-tube method are given in [36]. Once cool, the sample was removed from the drop-tube, weighed and sieved into the following size fractions: ≥ 850 μm, 850 - 500 μm, 500 - 300 μm, 300 - 212 μm, 212 - 150 μm, 150 - 106 μm, 106 - 75 μm, 75 - 53 μm, 53 - 38 μm and ≤ 38 μm.

XRD analysis was used to confirm that the drop-tube powders remained single-phase following rapid solidification processing. Subsequent to XRD analysis they were mounted and polished to a 1 μm surface finish for microstructural analysis. A 0.1 μm colloidal silica suspension was used for polishing samples for EBSD analysis. A Carl Zeiss EVO MA15 scanning electron microscope (SEM) was used for metallographic analysis. This was equipped with an Oxford Instrument X-Max Energy-Dispersive X-Ray (EDX) detector in order to check the chemical homogeneity of samples. Etching was performed using a mixture of equal parts HF, HCl and HNO_3. Samples were prepared for Transmission Electron Microscope (TEM) analysis using an FEI Nova 200 Nanolab focused ion beam (FIB), with the sections cut being approximately 10 μm × 7 μm and between 55-70 nm in thickness. Subsequent analysis was performed using a FEI Tecnai TF20 TEM. A FEI Quanta 650 FEGSEM with Oxford/HKL Nordlys EBSD system was used to perform Electron backscatter diffraction (EBSD) analysis on unetched samples.

3. Observation of Dendrite Fragmentation

Figure 1a shows an SEM micrograph of a polished and etched sample from the 150 – 106 μm sieve fraction. The sample exhibits a classic dendritic structure as observed in as-solidified samples of many alloys, with multiply impinging dendrites displaying a variety of orientations. Little evidence of fragmentation is apparent, although any such evidence may be obscured by the high density of impinging features.

Despite the clear differential etching between the dendritic features and the background matrix, the material is confirmed by XRD (not shown) as single phase β-Ni_3Ge, with all diffraction peaks being reliably indexed to ICCD reference pattern 04-004-3112, not only for the 150 – 106 μm sieve fraction shown in Figure 1a, but also for the other size fractions that will be discussed subsequently. As β-Ni_3Ge is a congruently melting intermetallic with a narrow homogeneity range the differential etching observed in Figure 1a would not be expected to arise

due to chemical inhomogeneity (partitioning of solute) during growth. To confirm this Figure 1b shows an EDX line scan perpendicular to a primary dendrite trunk, encompassing both dendritic and matrix material. The Figure confirms that the material is chemically homogenous with a composition consistent with β-Ni_3Ge, to within the normal error limits associated with the technique. Similar results were found using both line and area EDX scans on samples from all sieve fractions.

Given that both the etched, and unetched, material are the same phase with the same composition, the question arises as to what difference is giving rise to the differential dissolution that reveals the dendritic features observed. In [32] we perform TEM selected area diffraction analysis on both the dendrites and the featureless background material, demonstrating that the featureless background material is the ordered $L1_2$ variant of β-Ni_3Ge, while the dendritic features are the disorder fcc variant. This is revealed by the clear presence on superlattice spots from areas of featureless matrix and their corresponding absence in the dendrites revealed by etching. We therefore conclude that etching is revealing features that differ in respect to the extent of chemical ordering present.

As such, we may postulate a plausible model for the contrast revealed during etching as follows: Melt undercooling is favoured by rapid cooling and by the melt being divided into numerous small droplets. At some temperature, T_N, nucleation occurs which initiates the recalescence phase of solidification. Rapid dendritic growth occurs, leading to disorder trapping in the solid formed during recalescence. Conversely, relatively slow, near isothermal, solidification occurs in the residual liquid post-recalescence, with the solidification rate being determined only by the macroscopic heat extraction rate. Given that chemically ordered intermetallic compounds are known for their high degree of chemical resistance, it is likely that disorder trapping reduces the chemical resistance, leading to the differential contrast observed. Crucially, this gives a mechanism by which the rapidly solidified material formed during recalescence can be distinguished from the material that grew close to equilibrium in the post-recalescence period. As far as we are aware, this material is unique amongst congruently melting alloys in possessing this quality of permitting material that grew during the recalescence phase of solidification to be distinguished in the as-solidified sample from material that grew post-recalescence, without reference to structures originating from partitioning.

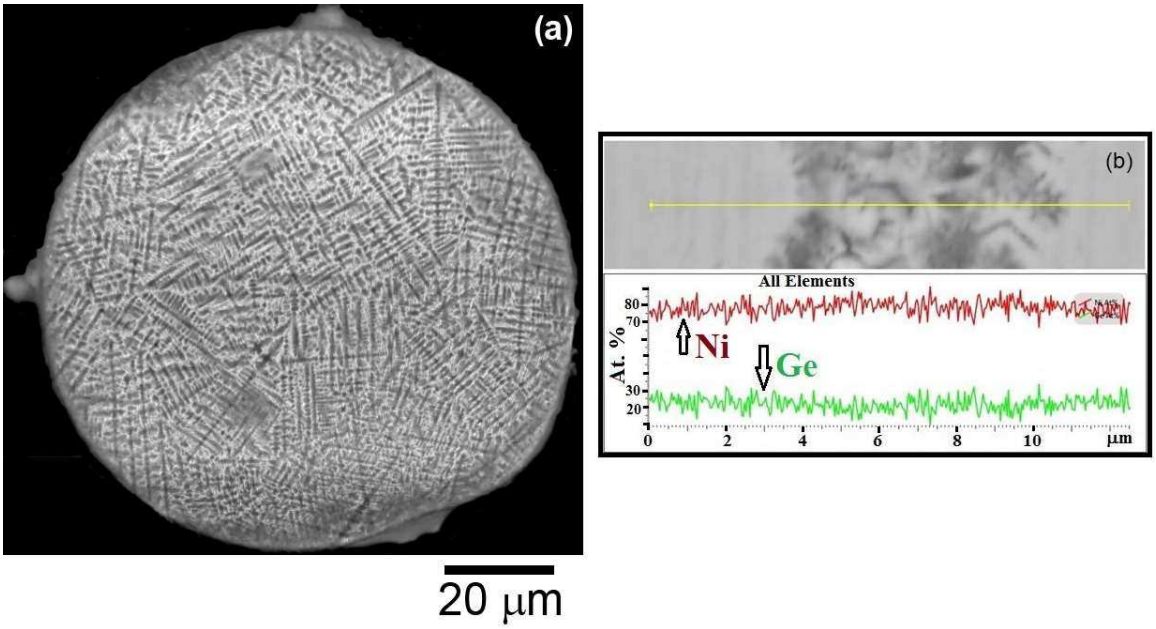

Figure 1. (a) SEM micrograph of an HF etched, drop-tube processed, Ni_3Ge droplet from the 150 – 106 μm sieve size fraction. Multiple dendrites are evident, displaying little evidence of fragmentation (b) EDX line scan across detail of dendrite arm showing chemical similarity of dendrite and matrix.

Evidence for the fragmentation of dendrites can be clearly seen from the SEM images shown in Figure 2. In Figure 2a (300-212 μm sieve fraction), numerous long straight lines of spherical fragments, typically 5-10 μm in diameter, can be seen. We conjecture that the most plausible mechanism to produce such a linear array of spherical elements is if they originally grew as a linear feature, i.e. a dendrite, which has then experienced remelting and spheroidisation. In particular, as indicated by the arrows in part (a) of the figure, we see what appears to be secondary dendrite arms projecting orthogonally from a line of spherical particles, almost certainly a fragmented primary dendrite trunk. The morphology highlighted here is very similar to that in [27 (see their Figure 1b)] where secondary dendrite arms projecting orthogonally from an almost completely fragmented and spheroidized primary trunk are also observed. In either case it is difficult to conceive that the observed linear arrays of spherical particles arise from sectioning effects and we are inclined to the view that these genuinely originate from dendrite fragmentation.

However, perhaps the clearest evidence of dendrite fragmentation can be seen in Figure 2 b-c, which is taken from the 212 – 150 μm sieve fraction. Here we see a clearly delineated dendrite which appears to have been frozen partway through fragmentation. The topmost side-branch on

the left-hand side of the primary trunk has become detached and has broken into several near spherical fragments, each with a diameter comparable to nearby intact side-branches, while the branch immediately below this one is displaying a well-developed spheroidising instability but has not managed to completely fragment. Similarly, on the lower right-hand side (Figure 2c only) there are further detached side-branches, also with well-developed spheroidising instabilities. Furthermore, a number of fully detached, isolated fragments are evident both to the upper left- and lower right-hand side of the primary trunk. The typical fragment size in Figure 5c-d is around 2.4 μm, wherein a very small grain size would be expected if each fragment were to result in a new grain.

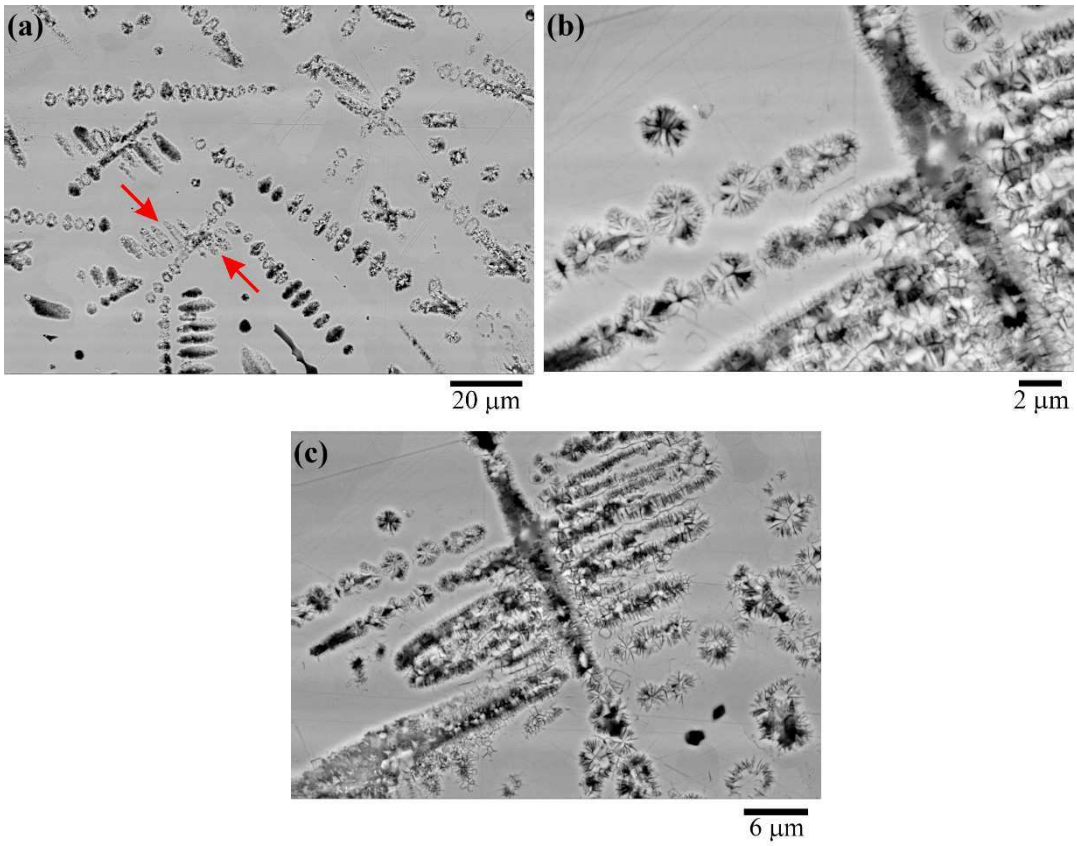

Figure 2. SEM micrograph of HF etched drop-tube processed Ni_3Ge droplets: **(a)** shows long straight lines of spherical fragments (300 – 212 μm sieve fraction) **(b)** detail from a dendrite in the 212 – 150 μm sieve fraction showing fragmented secondary dendrite arm and development of Rayleigh instabilities and **(c)** overview of the fragmented dendrite shown in (b).

The process giving rise to these morphologies we believe is as follows. Rapid cooling of the droplet during free-fall in the drop-tube leads to the melt undercooling by an amount $\Delta T = T_m - T_N$, where T_m and T_N are the melting and nucleation temperatures respectively. At T_N nucleation occurs and the droplet enters the recalescence stage of solidification, wherein there

is rapid growth of the dendritic morphology. Due to disorder trapping this grows as the disordered (fcc) variant of β-Ni_3Ge. During the post-recalescence plateau phase dendrite fragmentation occurs via the mechanism described above while the remaining liquid solidifies. As solidification of the post-recalescence residual liquid is much slower than during recalescence this grows as the ordered ($L1_2$) variant of β-Ni_3Ge, allowing the structure to be viewed after etching. The process is shown schematically in Figure 3.

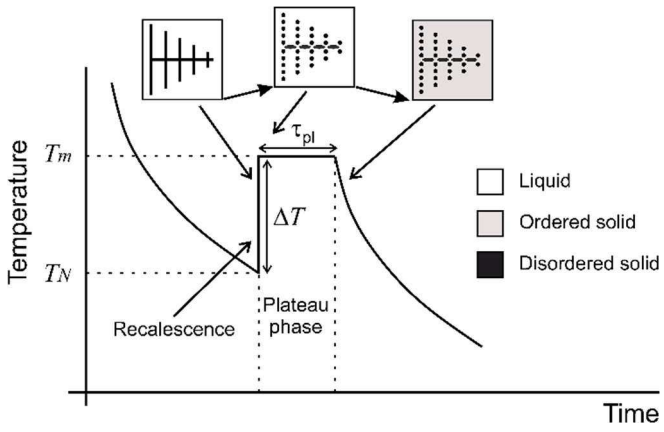

Figure 3. Schematic diagram showing the mechanism for microstructure formation in β-Ni_3Ge: (i) during the recalescence phase of solidification dendrites of the disordered (fcc) phase grow, (ii) during the plateau phase of solidification remelting and fragmentation of these dendrites occurs, (iii) slower post-recalescence is to the ordered ($L1_2$) phase, wherein fragmented dendrites of the disordered material are embedded within a matrix of the ordered material.

4. Calculation of Plateau and Break-up Timescales

4.1 Droplet Thermal History Estimation

The temperature evolution of a droplet of diameter, d, in free-fall may be determined by the balance of heat fluxes:

$$\frac{dT_d}{dt}\left[C_p - \Delta H_f \frac{df}{dt}\right] = \frac{6}{\rho d}\left[h\left(T_d - T_g\right) + \varepsilon\sigma_b\left(T_d^4 - T_g^4\right)\right] \qquad (1)$$

where T_d is the instantaneous temperature of the droplet, T_g the temperature of the gas through which the droplet is falling, f the instantaneous solid fraction in the droplet, C_p the specific heat, ΔH_f the heat of fusion, ρ is the density of the material, ε its surface emissivity and σ_b the Stefan–Boltzmann constant. Here for simplicity we take both C_p and ρ to be identical in the solid and liquid states. h is the convective heat transfer coefficient, which is given by [37] as:

$$h = \frac{\kappa_g}{d}\left[2 + 6\sqrt{\mathrm{Re}}\sqrt[3]{\mathrm{Pr}}\right] \tag{2}$$

Here, κ_g is the thermal conductivity of the gas while Re and Pr are the Reynold and Prandtl numbers for the flow, which are given by:

$$\mathrm{Re} = \frac{d\rho_g}{\mu}\left|u_d - u_g\right| \qquad \mathrm{Pr} = \frac{\mu C_{pg}}{\kappa_g} \tag{3}$$

where ρ_g, C_{pg} and μ are the density, specific heat and kinematic viscosity respectively for the gas through which the droplet is falling and $|u_d - u_g|$ is the relative velocity between the droplet and the gas.

In order to model the velocity of the falling droplet we assume, for drop-tube processing, that the droplet falls with terminal velocity through an otherwise stationary gas. Terminal velocity for a sphere of diameter, d, is given by:

$$\left|u_d - u_g\right| = u_T = \sqrt{\frac{4gd}{3C_d}\left(\frac{\rho - \rho_g}{\rho_g}\right)} \tag{4}$$

where C_d is the drag coefficient, which may be estimated from:

$$C_d\,\mathrm{Re}^2 = \frac{4mg\rho_g}{\pi\mu^2} \tag{5}$$

with m being the mass of the droplet.

To calculate the full thermal history of a droplet we also require knowledge of the undercooling at nucleation, ΔT, as this will determine fraction solid, f_r, formed during recalescence. For a given bulk cooling rate, the higher f_r the shorter will be the plateau time, as there will be less residual liquid to solidify. However, in drop-tube processing the nucleation temperature, T_N, at which solidification is initiated, and hence the growth undercooling, ΔT, cannot be measured for individual droplets as they are part of a dense cloud of such droplets, all of which are in free-fall. Consequently, ΔT has to be estimated as a function of the droplet size. Generally, smaller droplets will experience a higher maximum undercooling, due both to their higher cooling rate and melt sub-division effects.

Undercooling as a function of droplet size for atomised melts has been modelled by Lee & Ahn [38]. Based upon classical nucleation theory for heterogeneous nucleation and assuming only one nucleation event per droplet they show that the nucleation temperature may be estimated from:

$$\frac{\Psi(\theta)}{T_N \Delta T^2} = \ln\left\{\Phi(T_N, \theta, d)\right\}. \tag{6}$$

with:

$$\Psi(\theta) = \frac{16\pi\gamma^3 T_m^2 f(\theta)}{3k_B \rho \Delta H_f^2}. \tag{7}$$

and:

$$\Phi(T_N, \theta, d) = \frac{\frac{\pi}{6} d^3 K_v \Delta T^3 T_N^2}{\Psi(\theta)\dot{T}_N \left(3T_m - T_N\right) + \left[\lambda_1 + \lambda_2 \left(T_N - T_g\right)\Delta T^3 T_N^2\right]} \tag{8}$$

where:

$$\lambda_1 = \frac{12\kappa_g}{\rho C_p d^2} \quad \text{and} \quad \lambda_2 \frac{6\lambda_1 \sqrt{\mathrm{Re}}\sqrt[3]{\mathrm{Pr}}}{10T_m} \tag{9}$$

Here γ is the interfacial energy between the solid and the liquid, k_B is the Boltzmann constant, and K_v is a volume nucleation rate. $f(\theta) = (2 - 3\cos\theta + \cos^3\theta)/4$ is the contact angle factor that describes the catalytic potency of a nucleating particle as a function of its wetting angle, θ, for heterogeneous nucleation. Unfortunately, some of these parameters, in particular K_v and θ, are difficult to know as they will depend upon the purity of the material used and the nature of the impurities present. Here we use the parameters as determined by Wang & Wei[39], who have performed an assessment of the above model for drop-tube processed, Ge containing melts. They find that in order to obtain good agreement with experiment, the wetting angle, θ, must be a function of the droplet size, with $f(\theta)$ modelled by $f(\theta) = a + b/d$, where a and b are constants, given in [39] as a = -0.0307 and b = 35.5212. Using the parameters as given in [39] we obtain the relationship between droplet diameter and undercooling for drop-tube processed material as shown in Figure 4. This in turn permits the full calculation of the thermal history of a droplet of arbitrary size, an example of which is shown in Figure 5, where the parameters for Ni_3Ge are given in Appendix 1. Here, we have taken a droplet of 200 μm diameter as an

example, wherein the nucleation undercooling is estimated as 220 K giving a solid fraction immediately after recalescence of 0.37 and a plateau time of 0.076 s.

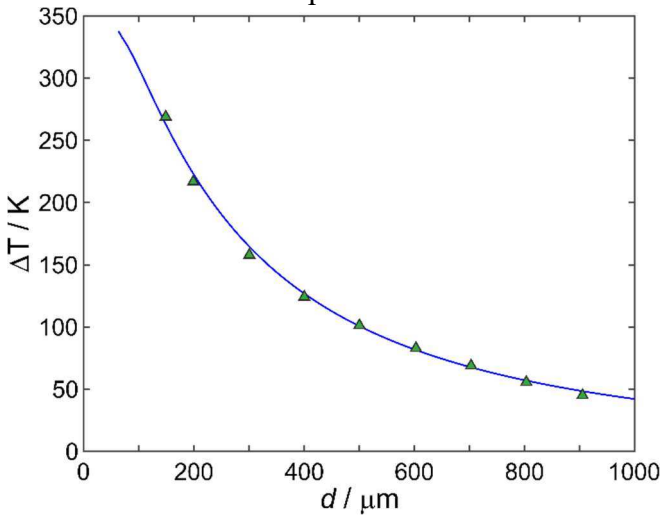

Figure 4. Estimate of the maximum undercooling achieved in drop-tube processed samples as a function of droplet size according to the model of Wang & Wei [39].

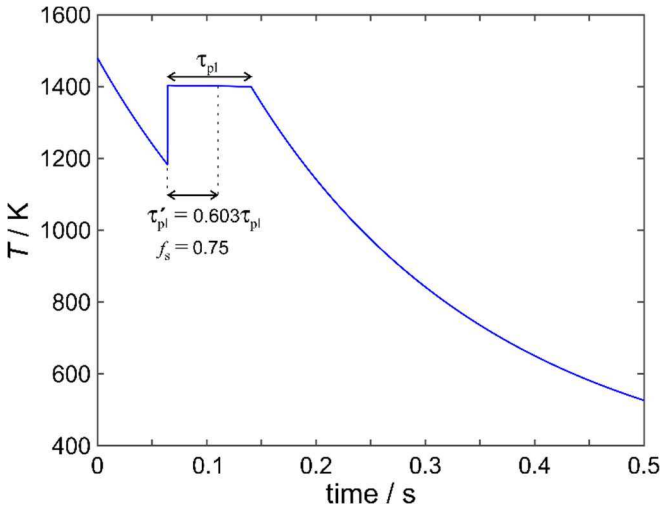

Figure 5. Calculated thermal history for a drop-tube processed droplet of 200 μm in diameter. The nucleation undercooling is estimated at 220 K, wherein the solid fraction immediately after recalescence is 0.37. The plateau time is 0.076 s.

4.2 Break-up Model for a Congruently Melting Compound

According to the model of Schwarz *et al*.[20], breakup is facilitated by the growth of a Rayleigh type instability, which they model as growing on an infinite cylinder of radius R, wherein they gave the amplification rate ω, for a perturbation with wave number k as:

$$\omega(k,R) = \frac{d_0 D_T}{R^3} f_1(kR)\left[\frac{1}{f_2(kR)} - \frac{m_l c_0 (1-k_E)}{\Delta H_f / C_p}\frac{D_T}{D_C}\right]^{-1} \tag{10}$$

where D_T and D_C are the thermal and solutal diffusivities, m_l the slope of the liquidus line, c_0 the notional composition of the alloy and k_E the equilibrium partition coefficient. d_0 is the capillary length, given by $d_0 = \Gamma/\Delta T_{hyp}$, where Γ is the Gibbs-Thomson coefficient and ΔT_{hyp} is the hypercooling limit. Here $\Delta T_{hyp} = \Delta H_f/C_p$ and $\Gamma = \gamma T_m/\rho\Delta H_f$. The functions f_1 and f_2 are given by:

$$f_1(kR) = \frac{kR\left[1-(kR)^2\right]K_1(kR)}{K_0(kR)} \tag{11}$$

$$f_2(kR) = \frac{1+K_0(kR)I_1(kR)}{K_1(kR)I_0(kR)} \tag{12}$$

Where I_j and K_j are order j modified Bessel functions of the first and second kind respectively.

In Schwarz *et al*.[20] the second term inside the square bracket in Equ. (10) is taken as much larger than the first term, which is ignored. Conversely, for the congruently melting Ni_3Ge compound, fragmentation will take place without the partitioning of solute, wherein the second term inside the square bracket in Equ. (10) will be identically zero. The function $f_1(kR)f_2(kR)$ has a maximum of 0.7657 at $kR = 0.533$, wherein following Schwarz *et al*. in writing τ_{bu} as the reciprocal of the maximum amplification rate we obtain for the congruently melting compound:

$$\tau_{bu}(\Delta T) = 1.3060\frac{R^3(\Delta T)\Delta H_f \Delta T_{hyp}}{\gamma D_T T_l} \tag{13}$$

Here, an infinite cylinder of radius R is being used to approximate the radius of the dendrite trunk, R_{trunk}.

4.3 Dendrite Size Estimation

To evaluate Equ. (13) above we require knowledge of the radius of the dendrite trunk, R_{trunk}. Following Schwarz *et al.*[20], this may be taken as a fixed multiple of the dendrite tip radius, R_{tip}, which in turn will be a function of the growth undercooling, ΔT. Using standard models for dendritic growth (e.g. [22]) we may write the total undercooling, ΔT, as the sum of the thermal, curvature and kinetic contributions, ΔT_t, ΔT_r and ΔT_k respectively, where these are given by:

$$\Delta T_t = \Delta T_{hyp} \mathrm{Pt} \exp(\mathrm{Pt}) \mathrm{Ei}(\mathrm{Pt}), \quad \Delta T_r = \frac{2\Gamma}{R_{tip}}, \quad \Delta T_k = \frac{V}{\psi} \tag{14}$$

where ψ is the kinetic growth coefficient, Ei is the exponential integral function and Pt is the Peclet number, given by:

$$\mathrm{Pt} = \frac{VR_{tip}}{2D_T} \tag{15}$$

The degeneracy in the solution expressed by Equ. (15) is broken by a relationship of the form:

$$R_{tip} = \frac{\Gamma}{\sigma^* \mathrm{Pt}\, \Delta T_{hyp}} \tag{16}$$

In marginal stability theory σ^* is a constant (= $1/4\pi^2$) which gives the wavelength of the smallest unstable perturbation to the solid-liquid interface[40], whilst in microscopic solvability theory[41] σ^* is an eigenvalue of the crystalline anisotropy strength, ξ. However, while the theoretical foundations of solvability theory are much sounder than that of marginal stability theory, the fact that ξ is unknown for the vast majority of materials, coupled with the fact that both models lead to an equation of the form of (16) means that, in practice, marginal stability is still widely used but with the condition that $\sigma^* = 1/4\pi^2$ relaxed. This is the approach that we have adopted here.

In order to apply the above dendrite growth model to determine R_{tip} we have used the velocity-undercooling data of Ahmad *et al.*[35] to constrain the model. Their data is shown in Figure 6. Two growth regimes were identified, kinetically limited growth of the ordered phase at low undercooling and free, diffusion limited growth of the disordered phase at high undercooling. It is the high undercooling data that we fit to here. As above, using the parameters in Table 1

for Ni_3Ge and taking $\sigma^* = 0.0193$ an acceptable fit is achieved, as shown in Figure 6. This in turn allows R_{tip} to be calculated, as shown in Figure 7.

The approach taken by Schwarz *et al.*[20] was to write $R_{trunk} = zR_{tip}$, thereby reflecting the self-similar nature of dendritic morphologies. In Schwarz *et al.*, z was taken as 20. Here, due to the isolated nature of the dendrites in the Ni_3Ge microstructures, direct measurement of the dendrite trunk radius is possible, wherein by comparison with the calculated tip radius given in Figure 7 we have arrived at the somewhat lower value of $z = 12$, which has been used in the calculation of the break-up time.

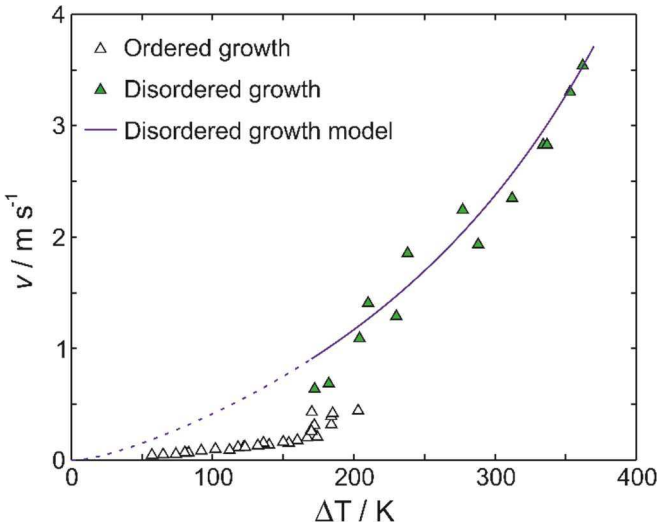

Figure 6. Velocity-undercooling data from Ahmad *et al.* [35] showing break in behaviour at a critical undercooling of $\Delta T \approx 168$ K, corresponding to the transition from ordered growth at low undercooling to disordered growth at high undercooling. Also shown is the growth model for the disordered phase presented here shown with a solid line for the temperature range for which it applies. Dotted line is the extrapolation of the disordered growth model to low undercooling wherein ordered growth is observed.

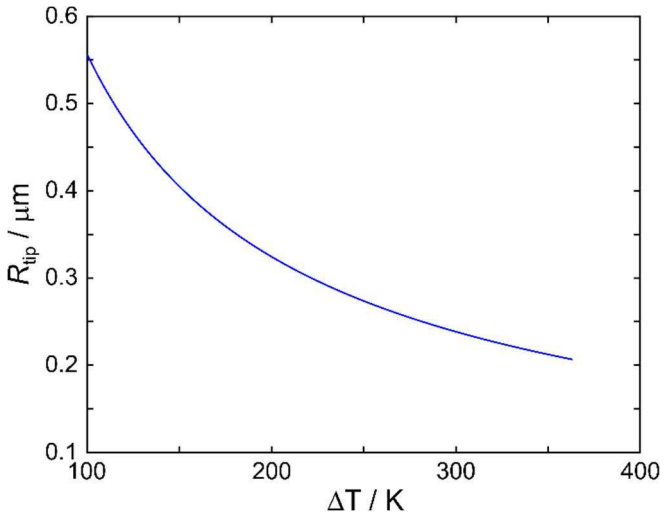

Figure 7. Calculated dendrite tip radius for the growth of the disordered solid as predicted by the model presented in Equ. (14)-(16).

4.4 Estimation of Dendrite Fragmentation

Equations (1)-(16) provide a complete description of the break-up and plateau times, which can now be combined to determine the size range over which fragmentation is to be expected. However, to make the comparison we first define a reduced plateau time, τ'_{pl}. The rationale for this is as follows: at the start of the plateau time the solid fraction is equal to the recalescence solid fraction given by $\Delta T/\Delta T_{hyp}$, for the case shown in Figure 5 this would be f_r = 0.37 corresponding to ΔT = 220 K. Conversely, at the end of the plateau time the solid fraction is 1, wherein it is clear that fragmentation cannot continue all the way until the end of the plateau. To account for this we have, somewhat arbitrarily, defined a reduced plateau time, corresponding to the point at which the solid fraction is equal to 0.75. This is consistent with the work of [42] who found that remelting mechanisms are less effective at high solid fraction and with that of Cline[21], who showed in regard to the spheroidization of rod like eutectics that at high solid fraction spheroidization is replaced by uniform coarsening along the length of the rod. We consider this to be an upper estimate of the point at which any fragmentation process is likely to be able to continue. The definition of the reduced plateau time is illustrated in Figure 5, with fragmentation terminating at the point indicated by τ'_{pl}. For the case shown here of a 200 µm diameter droplet, with an initial solid fraction at the end of recalescence of 0.37, the reduced plateau time is 0.603 of the full plateau time, or τ'_{pl} = 0.046 s.

The resulting estimates of the break-up and (reduced) plateau time are shown in Figure 8. The model predicts that, if dendrites are present, remelting and fragmentation will be expected for

all droplet sizes > 150 μm in diameter. This terminating limit for dendrite fragmentation agrees very well with the observed experimental evidence. Such fragmented dendrites appears to be the dominant morphology in the 300-212 μm sieve fraction, for which the break-up time is significantly less than the plateau time. In the next sieve size down, 212-150 μm, wherein the break-up and plateau times approach each other, partial fragmentation, particularly now of the secondary dendrite arm may still be observed, while for all smaller sieve fractions such fragmentation appears to be wholly inhibited by the high cooling rate. An example of this is shown in Figure 1 for the 150-106 μm sieve fraction.

The sensitivity of the model to the assumption of a reduced plateau time is indicated by the error bars in Figure 8, which are calculated to illustrate the effect of taking the reduced plateau time as being when the solid fraction is a low as $f_s = 0.65$ or as high as $f_s = 0.85$. With f_s as low as 0.65 the time available for fragmentation is reduced, moving the crossing point of the two curves to the right. In this case, all particles smaller than 235 μm in diameter would survive unfragmented. Conversely, if f_s were as high as 0.85 the time available for fragmentation is increased, moving the crossing point of the two curves to the left. In this case, only particles smaller than 112 μm in diameter would undergo fragmentation. However, in either case the level of agreement observed is sufficient to render the suggested mechanism plausible.

The model further assumes that solidification of each droplet is initiated from a single nucleation event. For such deeply undercooled melts this is normally a good assumption and we have no particular reason to doubt its validity here. Even if this were the case we believe the results would be insensitive to this. The effect of multiple nucleation events occurring in spatially separated locations would be to reduce the time taken for recalescence. However, as this is already very short relative to the plateau time, which is governed only by external heat extraction, the overall effect on the solidification time would be negligible.

For sieve sizes > 300 μm, the model of Wang & Wei[39] predicts that the maximum undercooling attained is < 168 K wherein, according to the data from Ahmad *et al*.[35], growth to the fully ordered compound is expected. Growth of the ordered compound is rate limited by kinetics, rather than diffusion, and as such dendritic morphologies would not be expected and the question of fragmentation no longer arises. In fact, this is exactly what is observed. For sieve fraction between 850-300 μm non-dendritic solidification morphologies are observed, with the dominant morphology being spherulites, as discussed in [43].

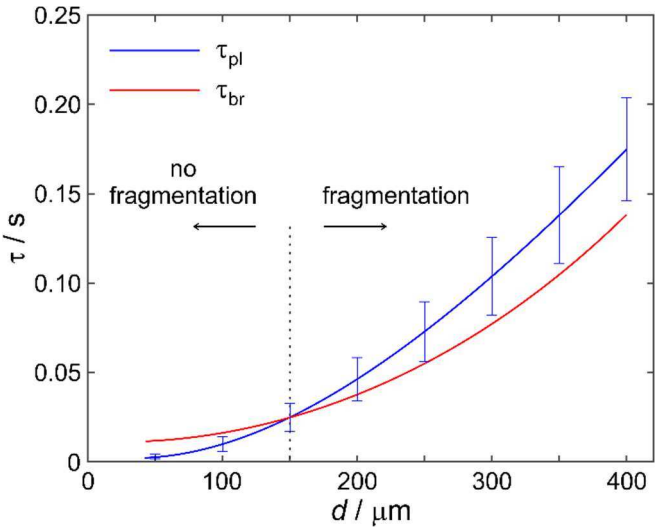

Figure 8. Estimates of the break-up and (reduced) plateau time for drop-tube processed Ni_3Ge. Dendritic fragmentation ($\tau_{pl} > \tau_{br}$) is predicted for droplets > 150 μm in diameter, but for droplets > 300 μm in diameter growth to the ordered $L1_2$ phase is predicted as insufficient undercooling is attained for disordered growth. For growth of the ordered phase non-dendritic microstructures are observed so fragmentation cannot occur.

Given that we can now, with reasonable certainty, conclude that dendritic fragmentation is occurring, the pertinent question becomes are these samples also grain refined.

5. Relationship between Dendrite Fragmentation and Grain Refinement

In order to investigate the relationship between fragmentation of dendrite side-branches and grain refinement, EBSD analysis was performed on freshly prepared samples that were polished using 0.1 μm colloidal silica and without etching. The use of EBSD is necessary as the etched samples do not display any contrast corresponding to grain boundaries. EBSD does not appear to be able to distinguish between the ordered and disordered variants of the β-Ni_3Ge compound in these samples, this seemingly being a consequence of the additional lines in the resulting Kikuchi pattern being relatively weak, coupled with the small spatial extent of the ordered features in these samples. In fact, we have shown elsewhere[43] that the ordered regions are only consistently distinguished from the disordered regions once their projection area approaches 300 μm^2 or greater. The previous XRD analysis, showing that all samples are single-phase β-Ni_3Ge is confirmed by the EBSD phase maps (not shown).

Figure 9 shows EBSD Euler maps (9a, 9c & 9e) and histograms (9b, 9d and 9f) for the 300-212 μm and 212-150 μm and 106-75 μm sieve fractions, corresponding to fully fragmented, partially

fragmented and non-fragmented dendrites respectively. The grain size distribution observed in the 300-212 μm sieve fraction, wherein complete dendrite fragmentation would be expected to give rise to extensive SGR, does not obviously conform to that expected. Indeed, the structure might be described in general terms as consisting of large grains which co-exist with much smaller grains, many of which appear to be embedded within the large grains. At the centre of the EBSD map we see a cluster of small grains. Taken in isolation, this region might be classified as being grain refined. However, radiating out from this are large (> 25 μm) grains, embedded within which are numerous very small (≈ 1-2 μm) grains. This would suggest that some fragments nucleate new grains but that many do not, instead becoming embedded within larger grains as they grow, possibly due to a low degree of misorientation if there was little movement of fragments following remelting. The distribution of grain sizes observed for the 212-150 μm sieve fraction is similar, although without the extensive embeding of small grains within larger ones that is observed in the 300-212 μm sieve fraction. Given the partial nature of the dendrite fragmentation taking place in this size fraction, and the reduced time for migration and reorientation of fragments that are formed, this is perhaps not surprising.

The corresponding distribution of grain misorientation is shown in Figure 9b & 9d. The majority of grain boundary misorientations are either < 10° or close to 60°. This is certainly not the MacKenzie distribution[44] that would be expected due to randomly nucleated grains, contrary to expectation if each fragment generated during remelting were acting as a nucleus to generate a new, randomly oriented, crystal. Indeed, a much more likely explanation is that there is little movement of fragments following remelting and that the dominant tendency is not to nucleate new grains but instead to be incorporated into existing growing grains with a small orientation mismatch. The small misorientations giving rise to such incorporation in to larger grains would be consistent with the results obtained for Al-Fe alloys by [24].

For comparison, we shown in Figure 9e the EBSD Euler map from a sample in the 106-75 μm sieve fraction, which is known to have a fully dendritic, unfragmented microstructure. The grain size is comparable to the sieve fractions that experience dendrite fragmentation but the distribution of grain misorientations (Figure 9f) is much closer to the MacKenzie distribution, suggesting multiple random nucleation sites within this sample. The large number of nucleation events apparent in the as-solidified sample would suggest that the disordered material comprising the dendrites that grew during the recalescence phase of solidification were relatively good nuclei for the ordered phase growing post-recalescence. This would tend to confirm that the lack of grain refinement in the samples with fragmented dendrites was due to

the small orientation differences between the fragments, rather than any inherent nucleation difficulty between the chemically ordered and disordered material.

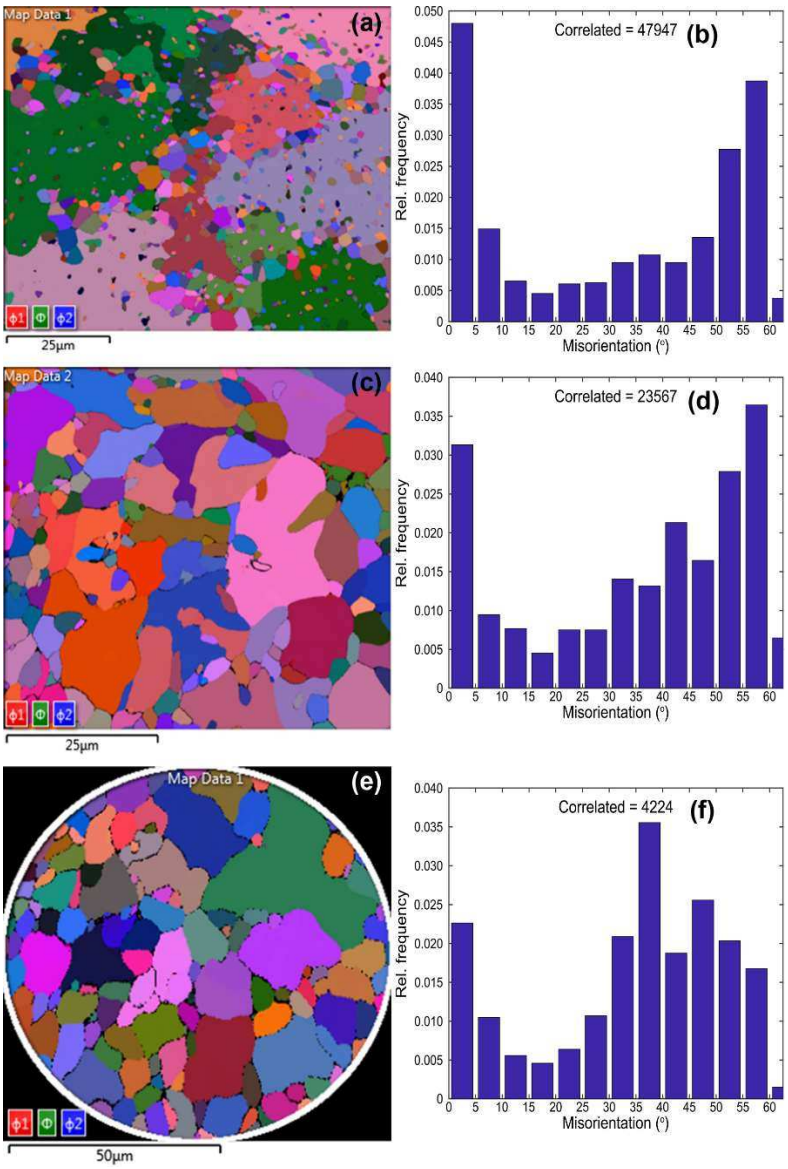

Figure 9. EBSD Euler texture maps of unetched Ni_3Ge drop-tube particles from (a) the 300-212 µm, (c) the 212-150 µm and (e) the 106-75 µm sieve fraction with (b, d & f) the corresponding histograms of grain misorientation.

Consequently our conclusion, based on the results presented here, is that dendrite fragmentation does appear to occur during the plateau phase of solidification following recalescence. Moreover, the structures observed, particularly at low recalescence solid fraction, appear indicative of breakup mediated by a Rayleigh instability, as suggested by [19, 20]. However, in

the drop-tube environment considered here, these fragments perform poorly as nuclei for new grains and the resulting grain structure is not that classically associated with spontaneous grain refinement. This may be because the relatively short duration of the plateau phase, coupled with the quiescent flow conditions prevailing within a droplet in freefall, does not favour movement of the fragments away from the site of their formation. It may be that in less quiescent environments, such as during terrestrial electromagnetic levitation (EML), where strong stirring has been shown to influence the results of undercooling experiment[45], remelting and fragmentation may produce a more uniformly grain refined structure. In this regard more comparative experiments between terrestrial EML and more quiescent techniques (drop-tube, melt fluxing and microgravity EML) are required.

6. Summary and Conclusions

A somewhat unusual property of the intermetallic compound β-Ni_3Ge has been identified which allows solid formed during recalescence to be distinguished from that formed post-recalescence. During equilibrium solidification β-Ni_3Ge will grow to the $L1_2$ order structure direct from the liquid. However, during rapid solidification disorder trapping results in growth to a random fcc solid solution. This disordered form is less resistant to chemical attack, wherein etching with a mixture of HF, HCl and HNO_3 preferentially dissolves the disordered material, allowing the recalescence structures to be distinguished from the infill material growing post-recalescence.

Via this mechanism we have been able to image a range of dendritic structures produced by rapid cooling of β-Ni_3Ge during drop-tube processing. A number of these, at the lower end of the available cooling rate range, show various degrees of fragmentation: from well-developed, isolated, spherical fragments to intact side-branches displaying the characteristic pattern of Rayleigh type instability prior to complete fragmentation. Where isolated dendrite fragments are observed these are typically small, 5-10 μm. As the cooling rate increases the density of dendrites revealed in the microstructure increases and the observable instances of fragmentation decreases. Both observations are consistent with theory, higher cooling rates (smaller particles) will lead to higher undercooling and hence a higher initial solid fraction, while the higher cooling rate will also decrease the plateau time, τ_{pl}, available for remelting.

EBSD mapping has been undertaken to determine the relationship between grain size and dendrite fragmentation. This reveals a far from clear cut relationship between dendrite fragmentation and grain refinement. In some cases clusters of small grains with sizes (≈ 2 μm

and upward) comparable to the observable fragments are evident, but these are typically intermixed with much larger grains of > 50 μm diameter. This does not conform to the typical pattern normally associated with spontaneous grain refinement. Moreover, a number of these large grains seem to have engulfed numerous small fragments with small crystallographic misorientations. This would suggest that spheroidised dendritic fragments of the type observed here are not necessarily good nuclei for the growth of new grains and that consequently dendrite fragmentation may be a poor mechanism for spontaneous grain refinement.

Acknowledgements

NH acknowledges financial support from Higher Education Commission (HEC) Pakistan and NED University of Engineering & Technology.

Declaration of Interests

Declarations of interest: none

References

[1] S.E. Battersby, R.F. Cochrane, A.M. Mullis, Growth velocity-undercooling relationships and microstructural evolution in undercooled Ge and dilute Ge-Fe alloys, *J. Mater. Sci.* **34** (1999) 2049.
[2] K.I. Dragnevski, R.F. Cochrane, A.M. Mullis, The mechanism for spontaneous grain refinement in undercooled pure Cu melts, *Mater. Sci. Eng. A* **375** (2004) 479.
[3] D. Li, K. Eckler, D.M. Herlach, Development of grain structures in highly undercooled germanium and copper, *J. Cryst. Growth* **160** (1996) 59.
[4] J. L. Walker, *The Physical Chemistry of Process Metallurgy Part 2*, ed G L St. Pierre, Interscience, New York, 1959, 845.
[5] R. Willnecker, D.M. Herlach, B. Feuerbacher, Evidence of nonequilibrium processes in rapid solidification of undercooled metals, *Phys. Rev. Lett.* **62** (1989) 2707.
[6] S.E. Battersby, R.F. Cochrane, A.M. Mullis, Highly undercooled germanium: Growth velocity measurements and micro structural analysis, *Mater. Sci. Eng. A* **226** (1997) 443.
[7] S.E Battersby, R.F. Cochrane, A.M. Mullis, Microstructural evolution and growth velocity-undercooling relationships in the systems Cu, Cu-O and Cu-Sn at high undercooling, *J. Mater. Sci.* **35** (2000) 1365.
[8] N. Liu, G. Yang, F. Liu, Y. Chen, C. Yang, Y. Lu, D. Chen, Y. Zhou, Grain refinement and grain coarsening of undercooled Fe–Co alloy, *Mater. Charact.* **57** (2006) 115.
[9] Y. Chen, F. Liu, G. Yang, N. Liu, C. Yang, H. Xie, Y. Zhou, Grain refinement of Fe75Ni25 alloys at low undercooling, *Mater. Charact.* **59** (2008) 412.
[10] T. Zhang, F. Liu, H. Wang, G. Yang, Grain refinement in highly undercooled solidification of Ni85Cu15 alloy melt: Direct evidence for recrystallization mechanism, *Scripta Mater.* **63** (2010) 43.

[11] G. Horvay, Freezing into an undercooled melt accompanied by density change, in: Proc. of the 4 US National Congress of Appl. Mech., Univ. California, 1962, pp. 1315-1325.
[12] T. Kattamis, M. Flemings, Solidification of highly undercooled castings, *Mod. Cast.* **52** (1967) 97.
[13] R. Schaefer, M. Glicksman, Direct observation of dendrite remelting in metal alloys, *AIME Met. Soc. Trans.* **239** (1967) 257.
[14] R.F. Cochrane, S.E. Battersby, A.M. Mullis, The mechanisms for spontaneous grain refinement in undercooled Cu–O and Cu–Sn melts, *Mater. Sci. Eng. A* **304** (2001) 262.
[15] K.I. Dragnevski, R.F. Cochrane, A.M Mullis, Experimental evidence for dendrite tip splitting in deeply undercooled, ultrahigh purity Cu, *Phys. Rev. Lett.* **89** (2002) 215502.
[16] A.M. Mullis, K.I. Dragnevski, R.F. Cochrane, The transition from the dendritic to the seaweed growth morphology during the solidification of deeply undercooled metallic melts, *Mater. Sci. Eng. A* **375** (2004) 157.
[17] E.G. Castle, A.M. Mullis, R.F. Cochrane, Evidence for an extensive, undercooling-mediated transition in growth orientation, and novel dendritic seaweed microstructures in Cu–8.9 wt.% Ni, *Acta Mater.* **66** (2014) 378.
[18] E.G. Castle, A.M. Mullis, R.F. Cochrane, Mechanism selection for spontaneous grain refinement in undercooled metallic melts, *Acta Mater.* **77** (2014) 76.
[19] A. Karma, Model of grain refinement in solidification of undercooled melts, *Int. J. Non-Equilibrium Process.* **11** (1998) 201.
[20] M. Schwarz, A. Karma, K. Eckler, D.M. Herlach, Physical mechanism of grain refinement in solidification of undercooled melts, *Phys. Rev. Lett.* **73** (1994) 1380.
[21] H. Cline, Shape instabilities of eutectic composites at elevated temperatures, *Acta Metall.* **19** (1971) 481.
[22] J. Lipton, W. Kurz, R. Trivedi, Rapid Dendrite Growth in Undercooled Alloys, *Acta Metall.* **35** (1987) 957.
[23] R. Heringer, Ch-A. Gandin, G. Lesoult, H. Henein, Atomized droplet solidification as an equiaxed growth model, *Acta Mater.* **54** (2006) 4427.
[24] J. Chen, U. Dahlborg, C.M. Bao, M. Calvo-Dahlborg, H. Henein, Microstructure evolution of atomized Al-0.61 wt% Fe and Al-1.90 wt% Fe Alloys, *Metall. Mater. Trans. B* **42** (2011) 557.
[25] P. Peng, X. Li, J. Li, Y. Su, J. Guo, H. Fu, Detachment of secondary dendrite arm in a directionally solidified Sn-Ni peritectic alloy under deceleration growth condition, *Sci. Rep.* **6** (2016) 27682.
[26] M. Huo, L. Liu, W. Yang, S. Hu, D. Sun, H. Su, J. Zhang, Dendrite growth and defects formation with increasing withdrawal rates in the rejoined platforms of Ni-based single crystal superalloys, *Vacuum* **161** (2019) 29-36.
[27] J.C. Hernando, E. Ghassemali, A. Diószegi, The morphological evolution of primary austenite during isothermal coarsening, *Mater. Charact.* **131** (2017) 492-499.
[28] E. Liotti, A. Lui, S. Kumar, Z. Guo, C. Bi, T. Connolley, P.S. Grant, The spatial and temporal distribution of dendrite fragmentation in solidifying Al-Cu alloys under different conditions, *Acta Mater.* **121** (2016) 384-395.
[29] N. Shevchenko1, H. Neumann-Heyme, C. Pickmann, E. Schaberger-Zimmermann, G. Zimmermann, K. Eckert, S. Eckert, Investigations of fluid flow effects on dendritic solidification: Consequences on fragmentation, macrosegregation and the influence of electromagnetic stirring, *IOP Conf. Ser.: Mater. Sci. Eng.* **228** (2017) 012005.

[30] G. Zeng, M.D. Callaghan, S.D. McDonald, H. Yasuda, K. Nogita, *In situ* studies evealing dendrite and eutectic growth during the solidification of Sn-0.7Cu-0.5Ag Pb-free solder alloy, *J. Alloys Compd.* **797** (2019) 804-810.
[31] H. Yasuda, K. Morishita, N. Nakatsuka, T. Nishimura, M. Yoshiya, A. Sugiyama, K. Uesugi, A. Takeuchi, Dendrite fragmentation induced by massive-like δ–γ transformation in Fe–C alloys, *Nature Comm.* **10** (2019) 3183.
[32] N. Haque, R.F. Cochrane, A.M. Mullis, Rapid solidification morphologies in Ni_3Ge: Spherulites, dendrites and dense-branched fractal structures, *Intermetallics* **76** (2016) 70.
[33] N. Haque, R.F. Cochrane, A.M. Mullis, Disorder-order morphologies in drop-tube processed Ni_3Ge: Dendritic and seaweed growth, *J. Alloys Compd.* **707** (2017) 327-331.
[34] A. Nash, P. Nash P *US National Bureau of Standards Monograph Series 25*, ASM Elsevier, Ohio (1976) 35.
[35] R. Ahmad, R.F. Cochrane, A.M. Mullis, Disorder trapping during the solidification of β-Ni_3Ge from its deeply undercooled melt, *J. Mater. Sci.* **47** (2012) 2411.
[36] O. Oloyede, T.D. Bigg, R.F. Cochrane, A.M. Mullis, Microstructure evolution and mechanical properties of drop-tube processed, rapidly solidified grey cast iron, *Mater. Sci. Eng. A* **654** (2016) 143.
[37] J. Szekely, N.J. Themelis, *Rate Phenomena in Process Metallurgy*, Wiley Interscience, New York 1972.
[38] E.-S. Lee, S. Ahn, Solidification progress and heat transfer analysis of gas-atomizer alloy droplets during spray forming, *Acta Metall. Mater.* **42** (1994) 3231.
[39] N. Wang, B.-B. Wei, Droplet undercooling during containerless processing in a drop-tube, *Chin. Phys. Lett.* **21** (2004) 1120.
[40] J.S. Langer, H. Müller-Krumbhaar, Stability effects in dendritic crystal growth, *J. Cryst. Growth* **42** (1977) 11.
[41] D.A. Kessler, J. Koplik, H. Levine, Pattern selection in fingered growth phenomena, *Adv. Phys.* **37** (1988) 255.
[42] A.M. Mullis, R.F. Cochrane, On the Karma model for spontaneous grain refinement at high solid fractions, *Int. J. Non-Equilibrium Process.* **11** (2000) 283-297.
[43] N. Haque, R.F. Cochrane, A.M. Mullis, Morphology of spherulites in rapidly solidified Ni-Ge intermetallics, *Crystals* **7** (2017) 100.1-12.
[44] J.K. MacKenzie, The distribution of rotation axes in a random aggregate of cubic crystals, *Acta Metall*. **12** (1964) 223.
[45] S. Binder, P. Galenko, D.M. Herlach, The effect of fluid flow on the solidification of Ni2B from the undercooled melt, *J. Appl. Phys.* **115** (2014) 053511

Appendix 1 – Parameters used in the Model

Quantity	Symbol	Value	Units
Properties of Ni_3Ge			
Specific heat capacity	C_p	575.3	J kg^{-1} K^{-1}
Latent heat	ΔH_f	346600	J kg^{-1}
Density	ρ	7297.5	kg m^{-3}
Melting temperature	T_m	1405	K
Thermal diffusivity	D_T	7.15×10^{-6}	m^2 s^{-1}
Emissivity	ε	0.2	
Solid/liquid interfacial energy	γ	0.2	J m^{-2}
Kinetic growth coefficient	ψ	$0.00574 + 0.00189V$	K s m^{-1}
Properties of N_2 Gas			
Thermal conductivity	κ_g	0.024	W m^{-1} K^{-1}
Density	ρ_g	1.165	kg m^{-3}
Specific heat capacity	C_{pg}	1039	J kg^{-1} K^{-1}
Viscosity	μ_g	1.76×10^{-5}	Pa s